Appl. Phys. B 81, 447–457 (2005)
DOI: 10.1007/s00340-005-1881-7

Applied Physics B
Lasers and Optics

K.-H. HONG[1,2,✉]
B. HOU[1]
J.A. NEES[1]
E. POWER[1]
G.A. MOUROU[1]

Generation and measurement of $>10^8$ intensity contrast ratio in a relativistic kHz chirped-pulse amplified laser

[1]Center for Ultrafast Optical Science and FOCUS Center, University of Michigan, 2200 Bonisteel Blvd., Ann Arbor, MI48109, USA
[2]Advanced Photonics Research Institute, Gwangju Institute of Science and Technology (GIST), 1 Oryong-dong, Buk-gu, Gwangju 500-712, Republic of Korea

Received: 21 December 2004 /
Revised version: 21 April 2005
Published online: 29 July 2005 • Springer-Verlag 2005

ABSTRACT We report on the generation and measurement of a $>10^8$ contrast ratio between main pulse and amplified spontaneous emission (ASE) from a relativistic kHz chirped-pulse amplified laser. We have enhanced the ASE contrast ratio as much as >400 times by employing a pulse cleaner composed of a μJ preamplifier and a saturable absorber. A third-order cross-correlator with a dynamic range of $>10^9$ and a scanning range of up to 4 ns has been developed for the contrast measurement. Detailed analysis of the cross-correlation trace shows that the random noise of spectral phase generates 20-ps pedestal structure starting from 10^{-6} level of the main pulse.

PACS 42.65.Re; 42.25.Kb

1 Introduction

Chirped-pulse amplification (CPA) laser technology in femtosecond regime has made it possible to realize high-power lasers producing relativistic intensity, specified by $>2 \times 10^{18}$ W/cm^2 for 800 nm wavelength, in small-scale laboratories. Recently, a typical sub-TW kHz CPA laser has become capable of delivering such a large intensity with the help of a laser focusing technique using high-numerical-aperture optics and a wavefront correction method [1]. We have called this type of laser "relativistic wavelength-cubed (λ^3)" laser because the relativistic intensity is obtained by localizing an amplified light temporally in the pulse duration of several cycles (spatially in several λ's) and spatially in the wavelength-limited spot size which corresponds to laser wavelength square (λ^2). The relativistic λ^3 regime defined by such a laser is technically very important for the study on relativistic light-matter interactions and other high-field sciences because it can be cost-effectively achieved by the modification of various sub-TW CPA lasers having a repetition rate from 10 Hz to a few kHz which are already developed at many laboratories and now are commercially available. The λ^3 concept can be also applied to >10 TW lasers to generate an intensity of $\sim 10^{22}$ W/cm^2 [2]. λ^3 studies also offer very high gradients and the possibility of generating isolated attosecond phenomena. For these practical reasons, relativistic studies in the λ^3 regime are expected to be accelerated.

It is well known that the intensity contrast ratio (ICR) between the main pulse and prepulses is an important factor in the application of a high-intensity laser to solid-target experiments because prepulses can generate unwanted plasmas before the main pulse arrives on the target. Usually there exist two kinds of prepulse in CPA lasers: femtosecond prepulses and ASE. The femtosecond prepulses originate from the imperfect isolation of amplified pulse from neighboring pulses. For example, the finite extinction ratio of a Pockels cell and polarizing optics induces incomplete pulse selection (or extraction in the case of a regenerative amplifier) against prepulses. In some high-gain multipass amplifier geometries, pulses leak from early passes owing to small-angle scattering from the gain medium, introducing prepulses. The strength and structure of femtosecond prepulses depends on the quality of optical components and the laser configuration, so the contrast ratio of these prepulses can be improved by removing the technical imperfections. As an example, the usage of two Pockels cells can enhance the contrast of the femtsecond prepulse up to 10^9 [3]. On the other hand, ASE is a general feature found in all the amplification systems operating based on population inversion process. In CPA lasers, it typically spans more than a few nanoseconds before the main pulse with an ICR of $10^4 - 10^6$. This level of contrast is not sufficient at relativistic intensity of more than 10^{18} W/cm^2 to avoid unwanted preplasmas generated via ionization. It has also been reported that nanosecond ASE with intensities as low as $10^8 - 10^9$ W/cm^2 can substantially affect the dynamics of laser-solid interactions through prepulse-heating and vaporization process [4]. Therefore, the ASE is a fundamental limiting factor in relativistic experiments and it should be kept as low as possible.

✉ Fax: +82-62-970-3389, E-mail: khhong@gist.ac.kr

Several techniques such as second-order autocorrelation [5], third-order cross-correlation [6–8], and plasma-shuttered streak camera [9] have been developed for the contrast measurement of mode-locked laser oscillators and high-peak-power (TW-class) CPA lasers. Measurements using these techniques have shown that the typical contrast ratios are $10^8 - 10^9$ with mode-locked lasers and $10^4 - 10^6$ with CPA lasers, respectively. Along with characterization techniques, much effort has been made to improve the ASE contrast ratio in high-peak-power CPA lasers. Second-harmonic generation [3, 10] can significantly enhance the ASE contrast ($>10^{10}$), but several parameters are adversely affected, such as conversion efficiency, spectral bandwidth, pulse duration, and wavefront distortion. High-energy clean-pulse injection method using preamplification with a saturable absorber has improved by 100 times the ASE contrast ratio, resulting in ICR enhancement from 10^5 to 10^7 [11]. Similar high-energy injection methods using a cavity-dumped oscillator [12] or a long-cavity oscillator [13] can also improve the ASE contrast ratio by one-order-of magnitude by reducing the total gain required for a given output energy. More recently, contrast-ratio enhancement by 2 and 3 orders of magnitude has been demonstrated using a double-confocal multipass amplifier scheme with 7-mJ pulse energy [14] and a double-CPA scheme with 1-mJ pulse energy [15], respectively.

Because of their relatively low peak powers, the ASE contrast in CPA lasers operating at kHz has received little attention so far even though, recently, 3 order of contrast-enhancement was achieved using nonlinear elliptical polarization rotation in a 850-μJ kHz CPA laser with a transmission of 25% [16]. However, the λ^3 concept operating at low-peak-power in kHz CPA lasers practically necessitates the measurement and enhancement of the ASE contrast ratio for their application to relativistic studies in λ^3 regime such as attosecond pulse generation [17], high-order harmonic generation, and electron acceleration [18, 19]. In this paper, we report the generation and characterization of $>10^8$ ASE contrast ratio from our relativistic kHz λ^3 laser [20]. Contrast-limiting factors other than ASE will be also discussed. In Sect. 2, we describe the laser configuration to enhance the ASE contrast ratio using a pulse cleaner composed of a μJ non-chirped preamplifier and a saturable absorber. In Sect. 3, a third-order cross-correlation measurement with a dynamic range of $>10^9$ and a scanning range of >4 ns will be presented for the contrast measurement. In Sect. 4, we will discuss the 20-ps pedestals shown in the third-order cross-correlation measurement in terms of the contrast-limiting factors such as spectral phase noise and spectral clipping. Sect. 5 provides a summary and conclusions for the results.

2 Configuration of a high-contrast relativistic kHz laser system

We have developed a high-contrast kHz relativistic laser by upgrading our previous kHz laser, which employed a conventional CPA technique with a multipass amplifier and a tight focusing method using an $f/1$ off-axis paraboloidal mirror and a deformable mirror for wavefront correction [1]. The upgrade emphasizes higher output energy as well as improved ICR. Two major changes in the laser are the installation of a pulse cleaner composed of a non-chirped preamplifer and a saturable absorber to engage the technique of high-energy clean-pulse seeding [11] and the addition of a cryogenically cooled 3-pass power amplifier, addressing contrast and energy, respectively. Figure 1 shows a schematic diagram of our high-contrast relativistic laser operating at a repetition rate of 0.5 kHz. The 2-nJ pulses generated in a mode-locked Ti:sapphire laser (FemtoSource Scientific Pro, Femto-Laser GmbH) are selected at 0.5 kHz with a Pockels cell (Fast Pulse, Lasermetrics Inc.) after a Faraday isolator (Faraday rotator BB8-10R, Electro-optic Tech Inc.). We have amplified the selected laser pulses without intentional stretching in a 6-pass preamplifier consisting of two curved mirrors with the curvature of 75 cm and 60 cm, respectively, and a Brewster-cut Ti:sapphire crystal pumped by the partial energy of a frequency-doubled Q-swithced Nd:YLF laser (Evolution-X, Spectra Physics Inc.). The two mirrors are set in the confocal geometry and the output beam after 6 passes propagates through a center hole in the mirror with 60-cm curvature, while the pump beam passes through the mirror with 75-cm curvature[1]. The output energy is limited by the wavefront distortion of the amplified femtosecond pulses due to high B-integral value, which is estimated to be ∼1 when the pulse energy is ∼6 μJ. Hence, we carefully adjust the pump power to extract as much energy as possible while monitoring the wavefront distortion using a Shack-Hartmann sensor (HASO, Imagine Optics Inc.). We obtain somewhat stable ∼1 μJ pulses with < 3 % root-means-squire (RMS) energy fluctuation at a pump power of 2.6 mJ even though the amplifier does not operate in saturation regime. The ICR of these laser pulses with a beam diameter of ∼2 mm is increased by focusing them on a 3-mm-thick saturable absorber (IR85 color filter, HOYA) using an $f = 10$ cm lens with a 2.7 times sacrifice of the pulse energy. We have observed with a photodiode that the transmission of the laser pulse through the saturable absorber is increased by 28 times as the saturable absorber is moved from the out-of-focus position to the on-focus position. This means the contrast ratio between high-intensity and low-intensity pulses is enhanced by 28 times. This enhancement factor is expected to become better after sequential amplifications as long as an excessive pump energy does not enhance ASE. In addition, we have also observed that the spatial beam quality is enhanced at the saturable absorber

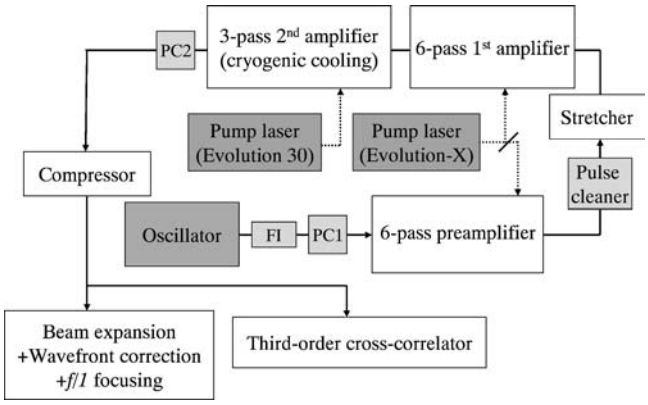

FIGURE 1 Configuration of the relativistic λ^3 laser operating at 0.5 kHz. FI, Faraday isolator; PCs, Pockels cells

because it plays the role as a spatial filter through intensity-dependent transmission. The saturable absorber which is a nonlinear filter does not increase the energy fluctuation because the transmitting part of the beam, i.e., the central part of the focused beam, is strong enough to have an almost constant transmission with intensity change ('saturation' regime of the saturable absorber).

After the pulse cleaning process, the laser pulses are stretched to 40 ps in a 2-grating stretcher and then amplified up to 7.0 mJ in 2 multipass amplifiers, as in a standard CPA laser. The first chirped-pulse amplifier has the same geometry and the same number of passes (6 passes) as the preamplifier. The rest energy from the frequency-doubled Q-switched Nd:YLF laser (Evolution-X), mentioned above, is used for pumping this amplifier and the Ti:sapphire crystal is water cooled. The pump energy ratio between the preamplifier and the first amplifier is adjusted using a waveplate/polarizer set so as to maximize the output energy with minimal ASE. The slightly saturated output energy from the first amplifier is 1.5 mJ with a pump energy of 7.0 mJ. The output beam is up-collimated using a telescope (two lenses) and sent to the second amplifier. It has a simple 3-pass geometry consisting of several 45° flat mirrors and a lens to optimize overlap between the amplified pulse and the pump beam at a Brewster-cut Ti:sapphire crystal. To minimize a thermal lensing effects in the Ti:sapphire crystal, we cool it to 130 K using a cryogenic cooler (CryoTiger, IGC Polycold Systems Inc.) in a vacuum chamber with two Brewster windows. This is necessary because the pump power from our frequency-doubled Nd:YLF laser (Evolution 30, Spectra Physics Inc.) is more than 10 W. The maximum output energy from the second amplifier is 7.5 mJ with a pump energy of 22 mJ. The laser pulse out of the second amplifier is expanded up to ∼5 mm by a telescope to protect mirrors and compressor gratings from optical damage and to avoid self-phase modulation in air after compression. And then, it passes through an additional Pockels cell combined with two polarizers not only for the suppression of femtosecond prepulses 9.2-ns ahead of the main pulse but also to block a back-reflected pulses generated from solid-target experiments. Photodiode measurement has shown that resultant contrast ratio of the prepulse at 9.2 ns is $\sim 10^6$. This contrast ratio is not negligible and will generate a certain amount of preplasma, but the time scale of 9.2 ns is long enough to allow us to neglect the plasmas generated by these prepulses. Due to the transmission efficiency of the Pockels cell and polarizer system, the input energy to the compressor is reduced to 6.0 mJ. The grating compressor has a diffraction efficiency of 50% and, thus, the final output energy of our laser system is 3.0 mJ.

Generated pulses have a spectral bandwidths of 43 nm centered at 805 nm and durations of 29 fs full-width at half-maximum (FWHM), measured using spectral interferometry for direct electric-field reconstruction (SPIDER). The laser beam is expanded up to >47 mm in marginal diameter and then focused down to 1.3 μm × 1.3 μm (FWHM) dimension with an $f/1$ off-axis paraboloidal mirror. The wavefront distortion induced in the entire laser system and the paraboloidal mirror is corrected by a deformable mirror via a genetic algorithm, which optimizes the second-harmonic (SH or 2ω) signal generated by the laser pulse in a thin β-BaB_2O_4 (BBO) crystal. The maximum intensity available at focus is estimated to be 4.7×10^{18} W/cm^2 because ∼60% of energy is concentrated on the spot size defined by FWHM. However, we actually get the intensity of 2.6×10^{18} W/cm^2 because of loss in delivery optics. This loss comes from two factors. The first one is over-magnification in the telescope, which expands the marginal beam diameter slightly more than 47 mm and induces beam clipping by the deformable mirror. The second is the accumulated reflection loss at 7 aluminum-coated mirrors including 2 spherical mirrors, 4 flat mirrors and a deformable mirror, and the protected-gold-coated paraboloidal mirror. This loss can be reduced to 10 % if we use a proper telescope and 6 dielectric-coated mirrors instead of the 6 aluminum-coated ones.

3 Measurement of ASE contrast ratio

For the measurement of ASE contrast ratio in the kHz relativistic laser described in Sect. 2, we have set up a third-order cross-correlator with a high dynamic range and a long scanning range as shown in Fig. 2. After the laser beam is divided at a thin beamsplitter, the transmitted beam is directed to the ω arm and the reflected one to the 2ω arm. The translation stage of the ω arm, driven by a step motor, has a travel range of 30 cm and makes it possible to scan up to 4 ns with a 4-pass scheme. The best resolution of the step motor is 5.3 fs with this scheme, but we have set the resolution at 53 fs to reduce a scanning time. In the 2ω arm, a 0.3-mm-thick type I BBO crystal is used to generate the 2ω-pulse and a color filter (BG12) blocks the residual ω pulse while transmitting the 2ω pulse (transmittance of 70 %) to prevent unwanted wave-mixing between the ω beams at the third-harmonic crystal. A manually adjustable translation stage in this arm confirms the zero delay position and allows an extra 200 ps scanning range. The third-harmonic generation (THG) is achieved by non-collinearly wave-mixing the two beams from ω and 2ω arms at a 0.3-mm-thick type II BBO crystal. We do not use a focusing geometry because the 3ω signal is strong enough to make a high-dynamic-range measurement. This makes the 3ω signal more robust over the long scanning range more than 4 ns. Background noise scattered from ω and 2ω beams and leaked from laboratory environment is removed using a beam dump, two fused silica prisms, a tube, and an ultraviolet (UV) filter at 266 nm, as illustrated in Fig. 2. We have changed the input polarization of the laser beam from horizontal to vertical using a periscope in order to obtain the 3ω pulse with a horizontal polarization, which is suitable for higher transmission of the UV beam through a prism. The 'background-free' 3ω signal is detected by a photo-multiplier tube (PMT; HC120-01, Hamamatsu Inc.) which is connected to a boxcar averager capable of gated integration (SR200 series, SRS Inc.) for higher dynamic range measurement. The 3ω signal is averaged over 10 shots for one step of the motor and then recorded at a computer with a digitization dynamic range of 13 bits.

The third-order cross-correlation signal should be properly attenuated for a high-dynamic-range measurement. Neutral-density (ND) filters calibrated at UV wavelength, i.e. 266 nm, are usually used for this purpose, but alternatively those calibrated at the fundamental wavelength, i.e. 800 nm,

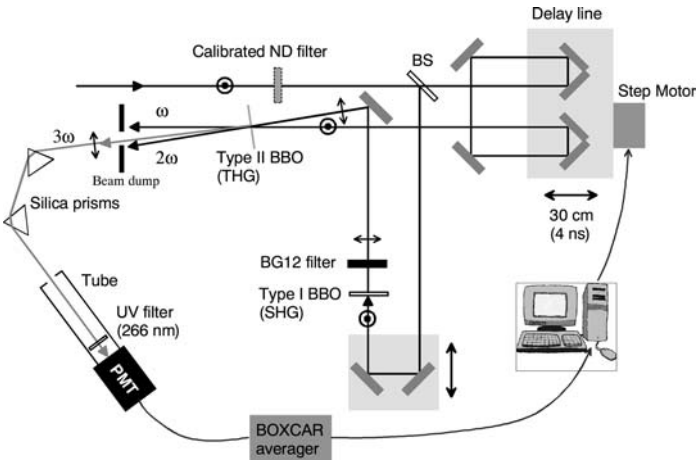

FIGURE 2 Setup of high-dynamic-range third-order cross-correlator. BS, beamsplitter

can be also used. In this scheme, the 3ω signal is attenuated according to the cubic law of the THG process at the cross-correlator, and thus, relatively weak (transmission of >0.1) ND filters are necessary because the attenuation factor for the 3ω signal is large even with a weak attenuation for the input laser beam. Weak ND filters at 800 nm wavelength can be calibrated with a good accuracy using a Ti:sapphire laser oscillator, which is a very stable light source. From this practical point of view, we have attenuated the input laser pulse instead of the 3ω correlation signal. Since the calibration error of our ND filters is less than 1 % at 800 nm, the calibrated 3ω correlation signal has an error less than 3 % by the cubic law, which is negligible in our high-dynamic-range measurement. We have also carefully checked the cubic dependence of 3ω intensity on ω intensity experimentally in our cross-correlator and found that it is well preserved within the energy fluctuation ($\sim$10 % in peak-to-valley; PV) of our 3ω correlation signal as long as the signal strength is below the saturation level of the PMT ($<$1 V at peak). In the experiment, we have increased the gain of the PMT up to the single-photon-counting regime to sensitively measure the ASE level, and attenuated the 3ω correlation signal at zero time delay, i.e., the strongest signal, using 3 ND filters whose transmissions are 0.315, 0.185 and 0.324, respectively. This filter combination provides the dynamic range of 8×10^6 from the cubic law. Considering that the experimental dynamic range of the boxcar averager is measured to be 1×10^3 despite the 13-bit digitization, we can estimate the instrumental limit of the dynamic range as 8×10^9. We have obtained 4 correlation data sets at around the zero delay using 4 different filter combinations: $0.315 \times 0.185 \times 0.324$, 0.315×0.185, 0.315, and no filter, respectively. A complete high-dynamic-range correlation is achieved by combining those 4 data sets. A full scan (-2.4 ns to 100 ps) is performed only for the measurement without any filter (the highest sensitivity), whereas partial scans from -100 ps to 100 ps are done with the other filter combinations because most of the femtosecond-duration peaks coming from inherent reflections inside the correlator appear within this time range.

To check the experimental dynamic range of our third-order cross-correlator, we have measured the background noise level under three conditions: without laser, with ω-arm blocked, and with 2ω-arm blocked. These three measurements are shown in Fig. 3. The lowest measurable correlation signal is at the level of 2×10^{-9} from the main pulse (dynamic range of 5×10^8), whereas the instrumental limit was at about 4×10^{-10} (dynamic range of 3×10^9). The instrumental limit is slightly less than but close to the estimated value (8×10^9). Thus, the main limiting factor of the experimental dynamic range is the leaked signal from the 2ω arm, which is believed to be scattered from the THG BBO crystal due to imperfection in its surface quality.

We have used a compressed energy of 2.0 mJ rather than full energy (3.0 mJ) to avoid any optical damage with the intracavity of the second pump laser, Evolution-30, due to a long and continuous operation. The pulse energy actually used in this measurement is less than 10% of this energy because of the clear aperture of the BBO crystals

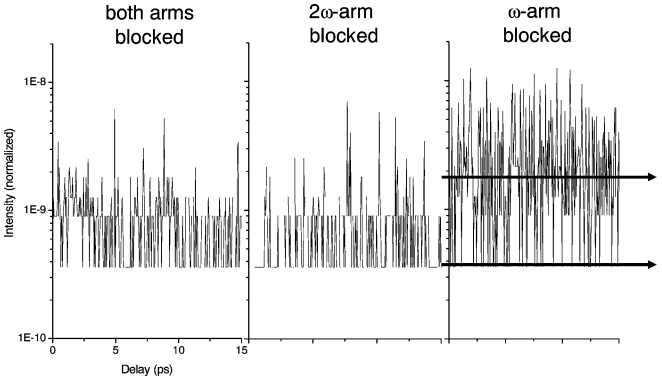

FIGURE 3 Measurement of various background noise levels of third-order cross-correlator

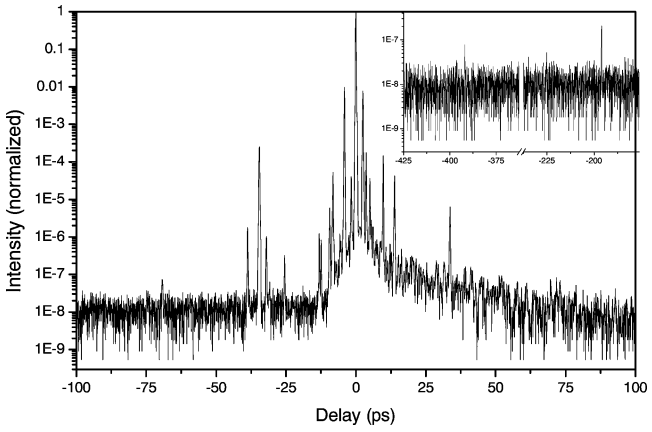

FIGURE 4 Third-order cross-correlation trace in the ±100 ps range measured for a laser pulse whose ASE contrast ratio is improved using high-energy cleaning-pulse injection method. The correlation trace shows 12 femtosecond-duration prepulse artifacts. The inset reveals 2 additional artifacts. *All* prepulse artifacts are traced to correlator reflections

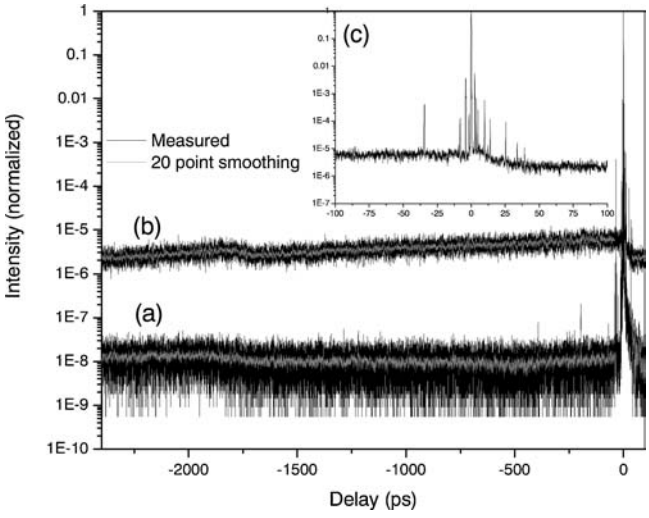

FIGURE 5 Third-order cross-correlation traces in nanosecond time scale. Trace **a** is the extension to −2.4 ps of Fig. 4, while trace **b** is measured with the laser pulses generated in a normal nJ-injection mode without a saturable absorber. The inset **c** shows the trace in the range ±100 ps of trace **b**. The 20-point smoothed traces (gray) show the ASE levels more clearly

(5 mm × 5 mm). It takes about 3 hours to get the scanning range from 100 ps to −2.4 ns. The measured third-order cross-correlation trace in the several hundred picosecond range is shown in Fig. 4. In this figure, we can observe several distinct features. First, we have found 12 compressed pulses within a −70 ps range and 2 more (inset of Fig. 4) at −196 ps and −392 ps, respectively. Second, the ASE level is at 1×10^{-8} relative to the main pulse. Third, an asymmetric >20-ps pedestal starting from 10^{-6} level appears. The last one will be discussed in Sect. 4. The first feature is an artifact commonly observed in high-dynamic range measurements using auto- or cross-correlators, but we have carefully identified these peaks to check if any real femtosecond prepulse exists. Nine of the peaks are identified in terms of multiple reflections of the main pulse at optical components such as beamsplitter (thickness of 0.37 mm), BG12 filter (thickness of 3.3 mm), and BBO crystal (thickness of 0.30 mm). The other five peaks are identified as artifacts coming from the real post-pulses generated at 2 waveplates and a Pockels cell in the laser system. A real post-pulse acts as a prepulse for the cross-correlation signal because it goes through 2ω arm with finite loss. Consequently, all the compressed prepulses are found to be artifacts and, thus, ASE is the only real prepulse energy that should be taken into account.

The ASE structure on the nanosecond scale (−2.4 ns to 100 ps) is shown in Fig. 5a, which is the extended cross-correlation trace of Fig. 4. The 20-point smoothed data, represented as gray lines, more clearly shows the background structure before and after the main pulse. The nanosecond background before the main pulse has signal level of 1.1×10^{-8} in the entire range, whereas the background signal level after the main pulse goes down to $\sim 8 \times 10^{-9}$ at 80 ps. The background reduction from gain depletion makes it sure that the nanosecond background before the main pulse is ASE. The root-mean-square (RMS) noise with the ASE level is 7.0×10^{-9}. Therefore, the intensity contrast ratio of our system is between 0.4×10^8 and 2.5×10^8 and the ASE is the limiting factor. The full ASE prepulse duration is restricted by the rising time of the second Pockels cell, which is <5 ns, and thus, it is estimated to be comparable to or slightly more than 5 ns. Since further scanning down to −4.2 ns (maximal scanning range) has shown that this ASE level is kept unchanged, the ASE contrast ratio is expected to be the same as or less than the measured value for the full ASE duration.

However, the actual ASE contrast ratio is better than measured value because of the pulse broadening of femtosecond peaks including the main pulse, prepulse artifacts, and post-pulses [22]. The pulse broadening effect mainly comes from the group velocity mismatch in the BBO crystals and the material dispersion in the ND filters, BG12 filter, beamsplitter and BBO crystals. Non-collinear geometry can also induce the pulse broadening, but in our case we have observed that the two prisms in Fig. 2 act as a narrow aperture for the 3ω signal. The alignment of two prisms is so sensitive that 3ω signal either is absorbed by the prisms or escapes from them if the beam path of 3ω signal is slightly deviated from the originally aligned one, along the horizontal plane, due to the non-collinearity. Thus, the non-collinear effect is almost negligible for the pulse broadening of correlation signal.

The FWHM of the femtosecond-duration pulses is measured to be 150−160 fs in the third-order correlation trace, but an ideal Guassian 29-fs pulse should yield a third-order correlated pulse duration of 35-fs considering the natural broadening factor of 1.22 [6]. Thus, the pulse broadening ratio for the femtosecond peaks is 4.3−4.6, and it roughly corresponds to the attenuation factor of the peak level of those pulses. This attenuation factor can be more accurately calculated by directly correlating ω pulse and 2ω pulse. The pulse duration of the ω signal is <40 fs considering the material dispersion, and that of the 2ω signal is estimated as ∼150 fs from the deconvolution of the measured third-order correlation signal. The large pulse broadening of the 2ω signal is mainly due to the group-velocity mismatch in two BBO crystals. Figure 6a–c show a 40-fs Gaussian pulse with a background level of 2.5×10^{-9} (ω pulse), a 150-fs one with a background level of 6.3×10^{-18} (2ω pulse) and the resultant 3ω correlation signal in delay axis (top), respectively. The

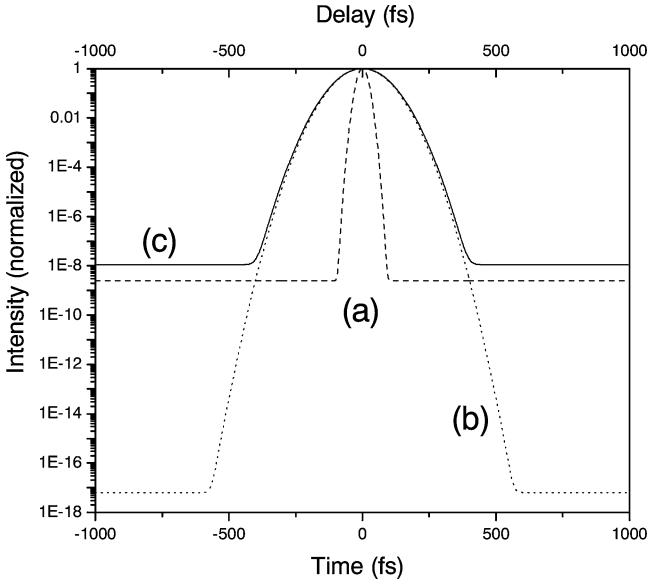

FIGURE 6 Simplified calculation of ICR attenuation factor due to the correlation process. A 40-fs Gaussian ω-pulse **a** with background at 2.5×10^{-9} and a 150-fs Gaussian 2ω-pulse **b** with background at 6.3×10^{-18} generate a 155-fs 3ω correlation trace **c** with background at 1.1×10^{-8}. The x-axis for trace **c** is on top

3ω signal is found to have a background level at 1.1×10^{-8}, which closely matches the ASE level measured in our laser and 4.4 times larger than the background level of ω pulse. We have also observed that the attenuation factor becomes smaller as the broadening of pulse gets larger. Thus, the previous calculation based only on the pulse duration can overestimate the attenuation factor, but it is still effective in our cross-correlator because the pulse broadening at ω arm is small. Consequently, if we consider the attenuation factor, 4.4, our third-order cross-correlator has a dynamic range of $\sim 2 \times 10^9$ (out of 5×10^8) for ASE contrast measurement, and the actual ASE level is estimated to be $(2.5 \pm 1.6) \times 10^{-9}$, or its contrast ratio is between 2.4×10^8 and 1.1×10^9. The intensity of ASE is less than 8×10^9 W/cm^2 when the main pulse is focused with the intensity of 2×10^{18} W/cm^2. The energy contained in the ASE (up to 2.4 ns) is only 0.02% of the main pulse energy. To our knoweldge, this is the first demonstration of $> 10^8$ ASE contrast ratio with laser pulses with a relativistic intensity at kHz.

To measure the ASE contrast ratio enhancement obtained by using the high-energy clean-pulse injection method, we have performed the third-order cross-correlation of the laser pulse amplified without saturable absorber. There are two methods to come back to a normal nJ-injected CPA laser from our modified CPA laser configuration without changing the laser alignment. First, we can neglect the preamplifier by blocking its pump beam and, instead, putting all the pump energy of Evolution-X into the first chirped-pulse amplifier. This scheme, however, has not worked because 6 passes in the first amplifier are not enough to saturate the gain. Second, we can use the preamplifier with adjusted pump energy. When the saturable absorber is removed without changing the pump energy, we have observed that the ASE level increases even though we have 2.7 times higher input energy into the first amplifier. The degraded spatial quality of the laser pulse due to the absence of saturable absorber makes the overlap between the amplified pulse and pump beam at Ti:sapphire crystal slightly worse than before. As a result, the gain saturation occurs at lower amplified energy and extra pump power induces ASE. Thus, we have slightly decreased the power of Evolution-X so as to minimize the ASE and simultaneously to keep the gain saturation in the first amplifier. The output energy from the second amplifier is 20% less than before because of the reduced input energy to this amplifier and the slightly degraded spatial beam quality. However, we could obtain the same output energy, 4.5 mJ, by increasing the pump energy of the second amplifier by 2.5 mJ. As a result, we have simulated a conventional nJ-seeded one- or two-stage CPA laser with a gain of $\sim 10^6$.

Figure 5b shows the third-order cross-correlation trace of nJ-seeded laser pulses with a scanning range from -2.4 ns to 100 ps, where gray lines also represents a 20-point smoothed trace. The inset (Fig. 5c) is the trace between -100 ps and 100 ps, where the relaxation time of 50 ps after the main pulse is also observed due to the gain depletion. The ASE structure before the main pulse is clearly seen in nanosecond time scale. It gradually (almost linearly on a linear scale) increases from 2.3×10^{-6} (at -2.4 ns) to 6.0×10^{-6} (at -100 ps) with the RMS noises of 6.0×10^{-7} and 1.3×10^{-6}, respectively. If the attenuation factor, 4.4 is considered, those levels become 5.2×10^{-7} at -2.4 ns and 1.4×10^{-6} at 100 ps, respectively. Those values correspond to $\sim 10^6$ contrast ratio as observed in typical CPA lasers [6, 8]. The ASE from -2.4 ns to -100 ps contains the energy as much as 7.3% of that of the main pulse.

Contrast enhancement factor is evaluated by comparing two third-order cross-correlation traces, Fig. 5a and b, in the time range of <1 ns. This time range is chosen from following rough estimation. The density of plasmas generated from a solid target ($\sim 10^{23}$ cm^{-3}) rapidly decreases with plasma expansion. We assume that, after a laser pulse is focused on a solid surface with a diameter of 10 μm, overdense plasmas are generated in this area with a depth of 1 μm and then expand with a speed of 10^7 cm/sec [21]. The time required for the plasma density to become lower than the critical density at 800 nm wavelength (1.75×10^{21} cm^{-3}) is estimated to be 150−350 ps. Furthermore, the plasma density gets lower than 0.1 times the critical density with an expansion time of 300 ps−1 ns. Thus, the time range of <1 ns is a reasonable scale for the contrast ratio comparison. Since the average ASE level in the range from -1.0 ns to -100 ps is $(1.2 \pm 0.3) \times 10^{-6}$ with the attenuation factor being taken into account, the enhancement factor of the ASE contrast ratio is >400, which is >4 times better than the previous result (~ 100) obtained using the same (high-energy clean-pulse injection) method [22]. Higher enhancement factor probably comes from the use of a multipass amplifier as the first chirped-pulse amplifier instead of a regenerative amplifier.

4 Limiting factors in contrast ratio other than ASE: explanation of pedestal

As mentioned in Sect. 3, one of the interesting features in the third-order cross-correlation trace in Fig. 4 is the

pedestal covering more than ±20 ps range and starting at the level of 10^{-6} of the main pulse. This pedestal is clearly independent of ASE because it is buried by the ASE in the level of 10^{-5} and invisible, as shown in the low-contrast case of Fig. 5c. The attenuation factor, 4.4, will not be considered in this section because the analyses of this section will show that this pedestal consists of many femtosecond pulses. Similar pedestals within 50 ps range were also found in other measurements [11, 23] and have been qualitatively explained in terms of 'uncompensated residual phase.'[22] However, we need to systematically know the origin of this pedestal because it can be a limiting factor of contrast ratio in the ±50 ps range. Thus, two kinds of residual phase, i.e., high-order phase distortion and random phase noise, are considered and their effect on the contrast ratio is quantitatively investigated. Also, the spectral clipping effect is analyzed because it naturally limits the contrast ratio by inducing small ripples in time domain. We will also add a short comment on the asymmetric structure of the pedestal.

4.1 *Effect of high-order phase distortion*

We begin with the effect of high-order phase distortion such as third-, fourth-, and fifth-order phase terms on this pedestal. Since our spectrum and SPIDER measurements have a dynamic range less than 10^4, measured spectrum and spectral phase profile is not used in this analysis. Instead, an ideal Guassian spectrum with a spectral bandwidth of 43 nm (FWHM) centered at 800 nm, as shown in Fig. 7a, is used and the values of phase terms are chosen so as to keep the pulse duration at 29 fs as measured using SPIDER. The high-order phase terms cannot be arbitrarily large because the 29 fs is 1.5 times the transformed-limited pulse duration, implying that the compression is not far from perfect. The pulse profiles depending on the high-order phase terms are shown in Fig. 7b–e, where TOD, FOD, and FiOD represent the third-, fourth-, and fifth-order dispersion terms, respectively. Those phase terms change only the pulse shape within 3 ps range at the level of 10^{-9} from the main pulse. Several other combinations are also attempted but they yield the same basic features. A linearly chirped 40-fs pulse is shown in Fig. 7f. This pulse duration has been chosen by considering the pulse broadening of pulse as discussed in Sect. 3. The linear chirp does not change the contrast ratio and the addition of high-order phase terms represented by dotted line induces the similar feature as Fig. 7e. Moreover, all the picosecond pedestals in Fig. 7 do not abruptly appear in contrast to the experimental result of third-order cross-correlation. Therefore, a smooth high-order phase curve is not a limiting factor in the contrast ratio in ±20 ps scale.

4.2 *Effect of 'random' phase noise*

In a compressor or stretcher, noise of the surface flatness is directly converted to spectral phase noise because a laser beam is spectrally resolved on optics. This means that the surface quality of compressor and stretcher optics such as mirror and grating is important for the spectral phase noise, which reduces the temporal coherence of the main pulse and generates a noisy structure on its side. An experimental observation of the contrast ratio dependence on this factor in the range of 300 fs was once reported by Antonetti et al. [7]. However, we will present a more systematic analysis with various conditions in the range of 20 ps. The effect of noise frequency, noise amplitude, and the combination with high-order phase distortion is investigated.

First, the effect of phase noise frequency on the contrast ratio is analyzed. Since the surface quality of the optics used in the compressor and stretcher of our laser is λ/10 in terms of PV, we have calculated the pulse profiles with various phase-noise frequencies at the amplitude of λ/10. Figure 8a shows 4 different spectral noises with different frequencies and Fig. 8b is the resulting temporal structure. White noise (case A) generates constant background at $\sim 10^{-6}$ and relatively smooth noises with moderate frequencies (cases B and C) yield pedestals in ±10 ps range at 10^{-8} or 10^{-9}. In contrast, a low-frequency noise (case D) does not make a 20-ps pedestal at the level more than 10^{-10} because this kind of noise is similar to the high-order phase distortion considered in Fig. 7. We have found that these picosecond pedestals consist of many femtosecond pulses unlike ASE and they always appear in the presence of different shapes of phase noise with a moderate frequency (like cases B and C) even though the detailed pedestal structure depends on phase noise shape. Thus, those random noise structures can be a good explanation for the 20-ps pedestal observed in our third-order cross-correlation measurement. Second, we have tested the noise amplitude dependence. Figure 9a shows the level of pedestals with the noise amplitudes of λ/4, λ/10, and λ/40 for the noise frequency 'B' of Fig. 8. Smaller noise amplitude yields lower pedestal levels as can be easily expected. Among several combinations of the noise amplitude and the noise frequency, either the case of 'λ/40' with frequency 'B' in Fig. 9 or the case of frequency 'C' with 'λ/10' in Fig. 8b seems to be relatively well matched to our measurement, wherein the pedestal started from the level of 10^{-6}. Finally, we have combined the high-order phase distortion with the random phase noise. Figure 9b is the temporal shape of λ/40 case in Fig. 9a combined with an arbitrary high-order phase combination (TOD = 10^3 fs^3, FOD=10^5 fs^4, FiOD = -10^7 fs^5). The high-order phase distortion still affects the pulse shape in the ±5 ps range whereas the phase noise generates the same 20-ps pedestal. Thus, we can treat the two residual phase factors independently and only the 'random' phase noise causes the pedestal in the range of >10 ps. In addition, we have found that the spectral shape does not change the basic structure of those 20-ps pedestals because it is mainly related to the temporal shape of stronger part of the pulse (<1 ps range).

To quantify the surface roughness of the optics causing the spectral phase noise, we have measured the surface quality of two holographic gratings which were used in a pulse compressor. A shearing interferometer device [24] (SID4 wavefront sensor, PHASICS Inc.) is utilized for a high-spatial-resolution and high-dynamic-range measurement. This wavefront sensor has a transverse resolution of 30 μm and a dynamic range of λ/200 (RMS) to 150 λ (PV). We have used a collimated beam from a diode laser with a wavelength of 658 nm and compared the wavefront of the input beam with that of the 1st-order diffracted beam. The wavefront

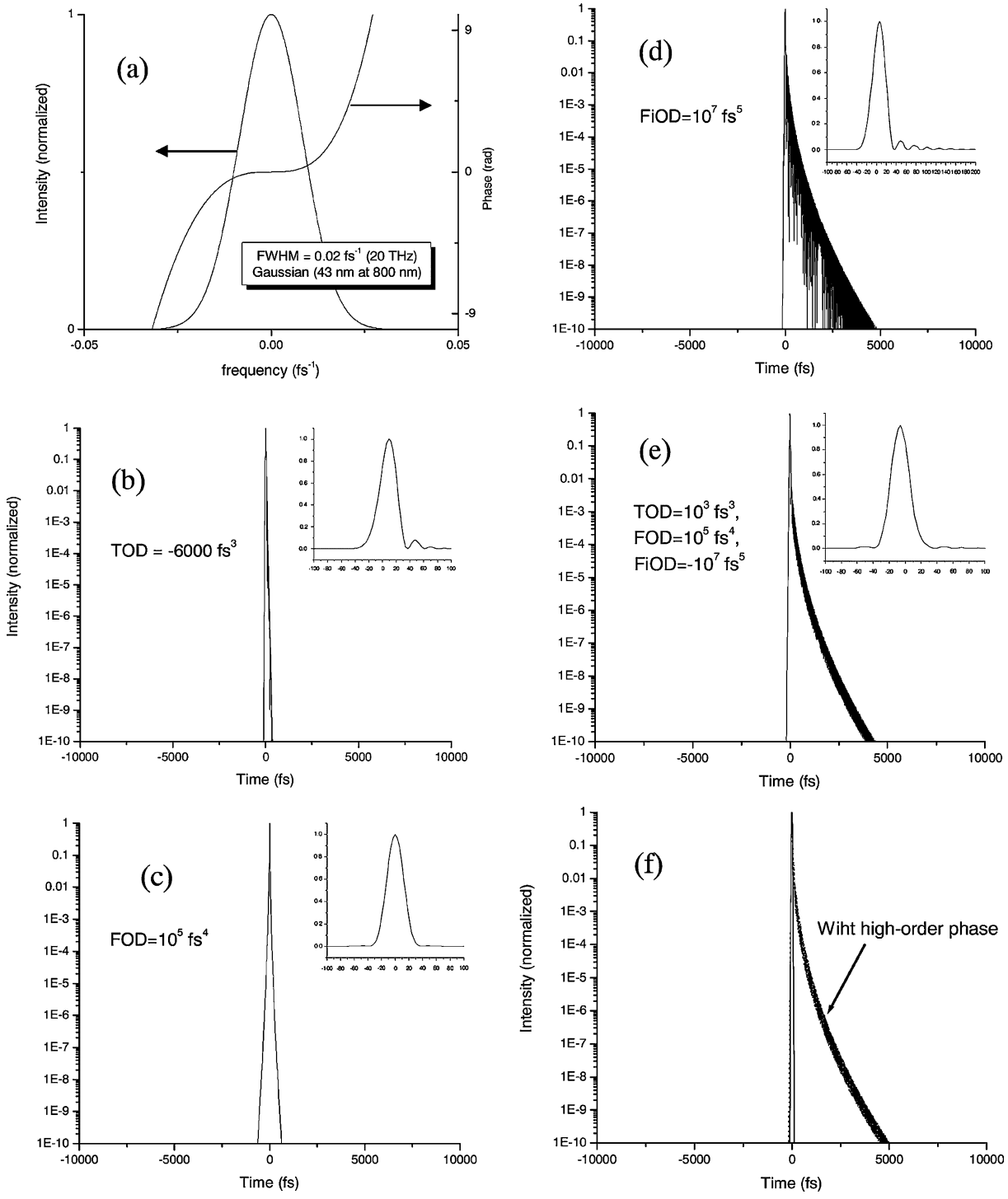

FIGURE 7 The effect of high-order phase distortion on contrast ratio. **a** Gaussian laser spectrum and a high-order phase curve (example). Temporal structure of various combination of high-order phase terms: **b** TOD $= -6000\,\mathrm{fs}^3$, **c** FOD $= 10^5\ \mathrm{fs}^4$, **d** FiOD $= 10^7\ \mathrm{fs}^5$, **e** TOD $= 10^3\ \mathrm{fs}^3$, FOD $= 10^5\ \mathrm{fs}^4$, and FiOD $= 10^7\ \mathrm{fs}^5$, and **f** chirped pulse with the pulse duration of 40 fs

difference corresponds to the surface roughness of the grating tested. Figures 10a and b show the measured surface roughness of two different holographic gratings. The 3-mm horizontal cross-sections for two gratings at the center part of the measured region are shown in Fig. 10c and d, respectively. The surface roughness is $\sim\lambda/10$ in PV and $\sim\lambda/60$ in RMS for both gratings even though the noise structure is different. The first grating (Fig. 10a) has a periodic phase noise probably generated during its manufacturing process, whereas the second one (Fig. 10b) shows more irregular feature. However, both gratings have high-frequency surface modulations that can cause the spectral phase noise in a pulse stretcher or compressor. Since the spectrally resolved beam at a grating in a stretcher or compressor typically occupies the dimension of several centimeters, the noise frequency shown in the case of 'B' or 'C' of Fig. 8a is reasonable. Based on

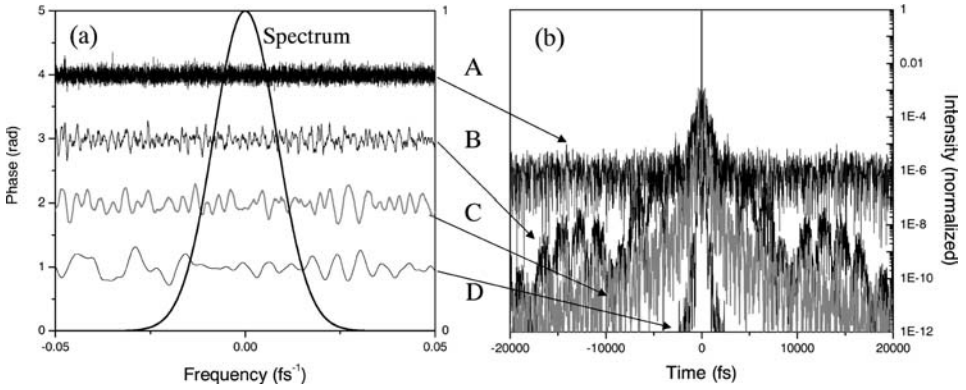

FIGURE 8 The effect of phase noise frequency on contrast ratio. **a** Laser spectrum and spectral phase curve with 4 different noise frequencies with the noise amplitude of λ/10. **b** Temporal structures corresponding to the phase curves A, B, C, and D

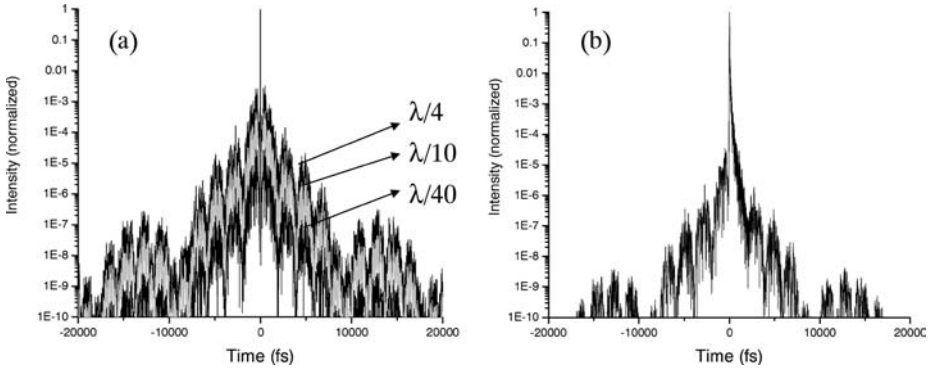

FIGURE 9 The effect of phase noise amplitude on contrast ratio **a** and the effect of phase noise combined with high-order phase distortion **b**

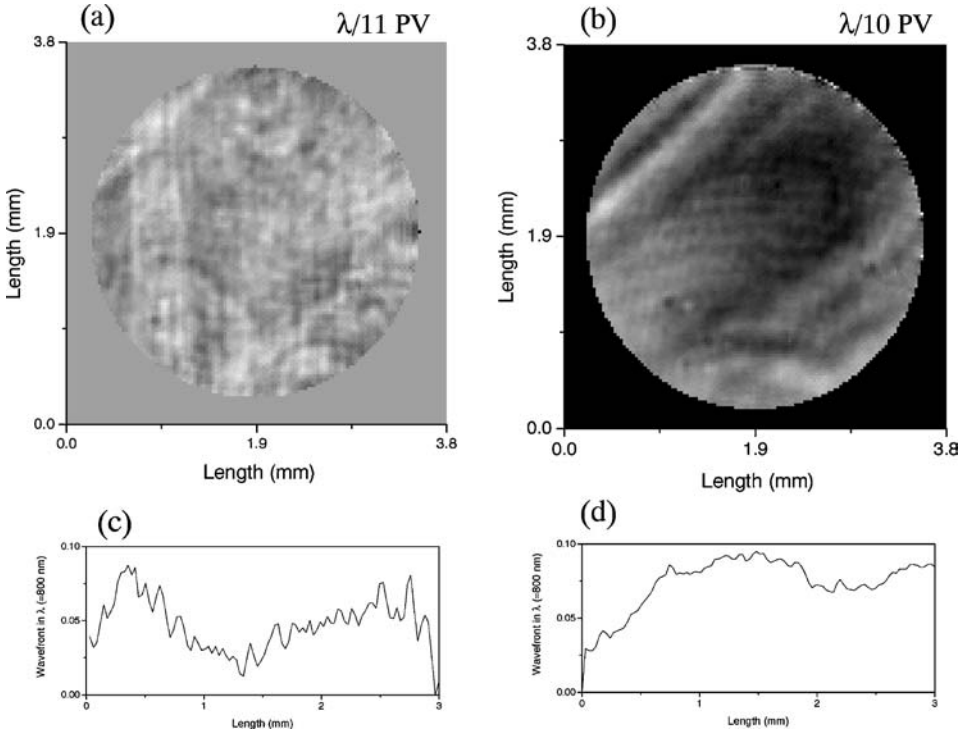

FIGURE 10 Measurement of surface roughness of gratings using lateral shearing interferometry. The wavefront distortions of the first-order diffracted beam from grating 1 **a** and grating 2 **b**, and corresponding line-outs **c** and **d**, respectively

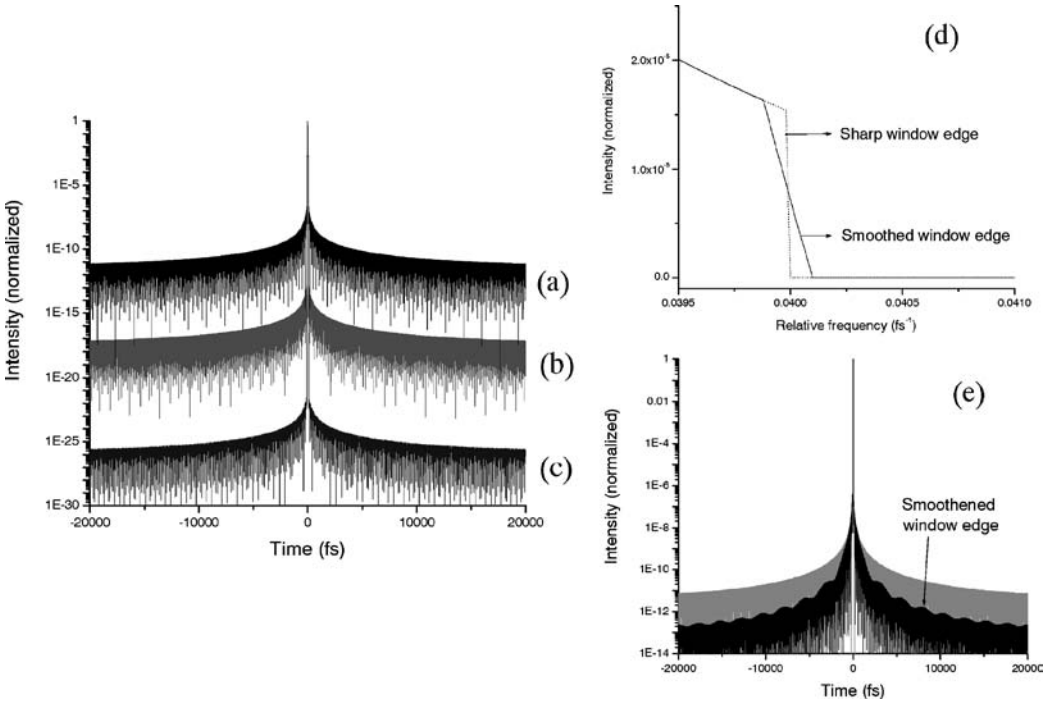

FIGURE 11 Spectral clipping effect on contrast ratio. The dependence of temporal structure on the bandwidth of 3 different spectral windows, i.e., 4 times the laser bandwidth **a**, 6 times **b**, and 8 times **c**. The spectral window edges with different sharpness **d** and resulting temporal structures **e**

the fact that no gratings used in CPA lasers have a perfectly smooth surface or diffraction wavefront, the spectral phase noise effect on the contrast ratio is unavoidable. This factor becomes significantly more important as the ASE contrast ratio gets higher.

4.3 *Effect of spectral clipping*

We have also checked the effect of spectral clipping [25] on the contrast ratio. Spectral windows with various widths from 4 times laser bandwidth (FWHM) to 8 times laser bandwidth have been applied to a Gaussian spectrum for Fourier transform, as shown in Fig. 11a–c. Narrower windows generated stronger ripples and poorer contrast ratio as expected. The spectral band of our CPA laser, limited by the stretcher and the compressor, is >4 times laser bandwidth, so the spectral clipping is not a main cause of 20-ps pedestal. Moreover, these ripples were strongly dependent on the sharpness of the spectral window edge. Figure 11d, for example, shows a smoothed edge of a Fourier transform window with 4 times laser spectrum bandwidth. In this figure, the spectral intensity of the window edge reduces from 1.6×10^{-5} to zero with a frequency change of 2.4×10^{-4} fs^{-1} (1 % bandwidth). The temporal profile for this condition is shown in Fig. 11e. The contrast ratio is reduced by much more than one order of magnitude at ±20 ps, whereas it remains unchanged in the region less than 1 ps. Spectral smoothing works as a low-pass filter in time domain, resulting in reduction of the pedestals far from the main pulse.

The spectral band edge of optics such as mirrors, Pockels cells, and polarizers is smooth, so the spectral clipping at either a stretcher or a compressor is deemed most important.

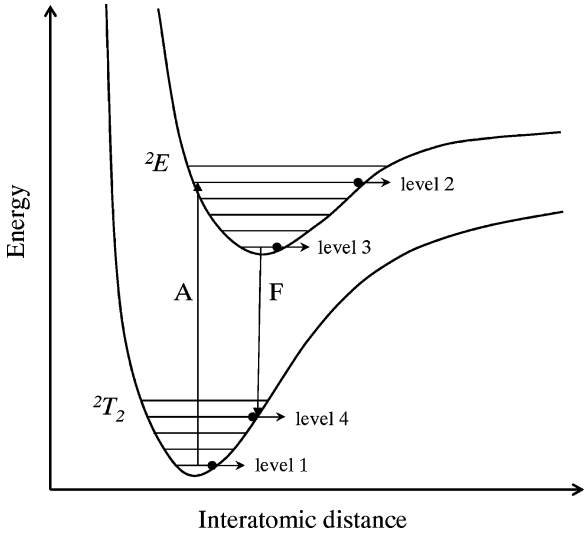

FIGURE 12 Schematic energy diagram of Ti:sapphire crystal

However, a compressor eventually smoothes the spectral window edge of laser pulses because the beam size in a compressor is relatively large compared to that in a stretcher. A large beam size induces a spatial dependence of a spectral window in the horizontal dimension of a grating or a retro-reflector and, thus, the spectral window edge will be smoothed because of the spatial averaging effect. Therefore, based on the example of Fig. 11e, 20-ps ripples are expected to be very weak whereas the ripples in <1 ps region can still be strong. Consequently, we believe that the 20-ps pedestals come from the spectral phase noise rather than from the spectral clipping. However, the spectral clipping is still an important issue for the design of high-contrast lasers.

4.4 *Asymmetric structure*

An asymmetry in the pedestal is clearly found in Fig. 4, where the falling time is about 80 ps while the rising time is only 20 ps. The 50-ps trailing part is also found in the low contrast case of Fig. 5b and the measurement done by Aoyama et al. [8]. Since the trailing part in those cases exists even without the 20-ps rising part, it is independent of the spectral phase noise and can be explained in terms of the relaxation process of gain depletion as follows. Figure 12 shows the schematic energy diagram of Ti:sapphire crystal based on Franck-Condon principle [26, 27], where the upper electronic energy curve is ^2E excited state and the lower one, $^2T_2$ ground state. Absorption (A) occurs between vibronic levels 1 and 2, while fluorescence (F) or lasing does between vibronic levels 3 and 4. Crystal field and electron-phonon coupling form the broad absorption and emission bands [28]. When the laser pulse is amplified in saturation regime, the population of level 3 is strongly depleted within the laser pulse duration and, as a result, the population inversion is expected to be broken immediately after the pulse passes through the gain medium. However, it takes a finite time for the electrons at level 4 to decay to the ground level 1, slowing down the depletion of the population at level 3. It means the residual emission between the levels 3 and 4 can occur until the decay process is finished. This nonradiative decay process is related to phonon transition, whose time scale is typically in the picosecond range [29]. From above discussions in this section, we believe that the asymmetry comes from the combination of those two phenomena, i.e., the phase-related pedestal and the gain depletion process related to the phonon transition in $^2T_2$ ground state. Detailed calculation on the phonon transition time is not attempted in this paper because the trailing part is regardless of the contrast ratio.

5 Summary and conclusions

We developed a high-contrast relativistic λ^3 laser operating at 0.5 kHz and measured an ASE contrast ratio using a high-dynamic range third-order cross-correlator. The third-order cross-correlation was performed up to 4 ns ahead of the main pulse, which clearly revealed the ASE structure. We observed >400 times enhancement of the ASE contrast ratio by employing a high-energy clean-pulse injection method and, as a result, the ASE contrast ratio, estimated from the measurement, was between 2.4×10^8 and 1.1×10^9. Other contrast-limiting factors such as high-order phase distortion, spectral phase noise and spectral clipping were discussed to explain the 20-ps pedestal structure. Based on the measurement of the grating surface roughness using lateral shearing interferometry, we concluded that the spectral phase noise generated in optics in a stretcher or compressor was the most probable factor causing the 20-ps pedestal. As the ASE contrast ratio gets even higher than 10^9, the spectral noise factor becomes more important because the pedestal can extend much more than 20 ps ahead of main pulse.

The high-contrast optical pulses generated in our relativistic λ^3 laser are a very efficient source for the study of relativistic light-matter interactions because they can be relatively easily produced in a small-scale laboratory with a high repetition rate. In addition, the analysis on the contrast-limiting factor will help to avoid problems in developing CPA laser systems with higher contrast ratio.

ACKNOWLEDGEMENTS The authors thank to Benoit Wattellier and Marie Begona Lebrun of PHASICS for their help in measuring the surface quality of the gratings. This work was supported by the NSF (FOCUS Program, Grant No. 0114336) and the ARO (Grant No. DAAD19-03-1-0287 and DAAD19-03-1-0316). K.-H. Hong would wish to thank Korea Research Foundation (KRF) for its support through the Post-doctoral Fellowship Program.

REFERENCES

1 O. Albert, H. Wang, D. Liu, Z. Chang, G. Mourou, Opt. Lett. **25**, 1125 (2000)
2 S. Bahk, P. Rousseau, T. Planchon, V. Chvykov, G. Kalintchenkov, A. Maksimchuk, G. Mourou, V. Yanovsky, Opt. Lett. **29**, 2837 (2004)
3 D.F. Price, R.M. More, R.S. Walling, G. Guethlein, R.L. Shepherd, R.E. Stewart, W.E. White, Phys. Rev. Lett. **75**, 252 (1995)
4 K.B. Wharton, C.D. Boley, A.M. Komashko, A.M. Rubenchik, J. Zweiback, J. Crane, G. Hays, T.E. Cowan, T. Ditmire, Phys. Rev. E **64**, 025401(R)(2001)
5 A. Braun, J.V. Rudd, H. Cheng, G. Mourou, D. Kopf, I.D. Jung, K.J. Weingarten, U. Keller, Opt. Lett. **20**, 1889 (1995)
6 S. Luan, M.H.R. Hutchinson, R.A. Smith, F. Zhou, Meas. Sci. Technol. **4**, 1426 (1993)
7 A. Antonetti, F. Blasco, J.P. Chambaret, G. Cheriaux, G. Darpentigny, C. Le Blanc, P. Rousseau, S. Ranc, G. Rey, F. Salin, Appl. Phys. B **65**, 197 (1997)
8 M. Aoyama, A. Sagisaka, S. Matsuoka, Y. Akahane, F. Nakano, K. Yamakawa, Appl. Phys. B **79**, S149 (2000)
9 A.-C. Tien, M. Nantel, G. Mourou, D. Kaplan, M. Bouvier, Opt. Lett. **22**, 1559 (1997)
10 Z. Jiang, J.C. Kieffer, J.P. Matte, M. Chaker, O. Peyrusse, D. Gilles, G. Korn, A. Maksimchuk, S. Coe, G. Mourou, Phys. Plasmas **2**, 1702 (1995)
11 J. Itatani, J. Faure, M. Nantel, G. Mourou, S. Watanabe, Opt. Comm. **148**, 70 (1998)
12 Y.H. Cha, K.H. Hong, C.H. Nam, Opt. Comm. **185**, 413 (2000)
13 J.H. Sung, K.-H. Hong, Y.H. Cha, C.H. Nam, Jpn. J. Appl. Phys. **41**, L931 (2002)
14 J. Wojtkiewicz, C.G. Durfee, Opt. Exp. **12**, 1383 (2004)
15 M.P. Kalashnikov, E. Risse, H. Schonnagel, A. Husakou, J. Herrmann, W. Sandner, Opt. Exp. **12**, 5088 (2004)
16 A. Jullien, F. Auge-Rochereau, G. Cheriaux, J.-P. Chambaret, P. d'Oliveira, T. Auguste, F. Falcoz, Opt. Lett. **29**, 2184 (2004)
17 N.M. Naumova, J.A. Nees, I.V. Sokolov, B. Hou, G.A. Mourou, Phys. Rev. Lett. **92**, 063902 (2004)
18 A. Mordovanaki, N. Nelson, B. Hou, J. Nees, N. Naumova, G. Mourou, in *CLEO/IQEC2004*, San Francisco, USA, 16–21 May 2004, JTuC
19 N. Naumova, I. Sokolov, J. Nees, A. Maksimchuk, V. Yanovsky, G. Mourou, Phys. Rev. Lett. **93**, 195003 (2004)
20 K.-H. Hong, B. Hou, J.A. Nees, E. Power, G.A. Mourou, CLEO/QELS 2005 (Baltimore, USA 21–27, May 2005), oral presentation JFA2
21 William L. Kruer, *The Physics of Laser Plasma Interactions* (Addison-Wesley Publishing Company, USA, 1988)
22 M. Nantel, J. Itatani, A.-C. Tien, J. Faure, D. Kaplan, M. Bouvier, T. Buma, P.V. Rompay, J. Nees, P.P. Pronko, D. Umstadter, G.A. Mourou, IEEE JST QE **4**, 449 (1998)
23 P. Rousseau, private communication about the third-order correlation measurement at HERCULES laser, University of Michigan
24 J. Primot, L. Sogo, J. Opt. Soc. Am. A **12**, 2679 (1995)
25 G. Cheriaux, P. Pousseau, F. Salin, J.P. Chambaret, B. Walker, L. Dimauro, Opt. Lett. **21**, 414 (1996)
26 B.F. Gächter, J.A. Koningstein, J. Chem. Phys. **60**, 2003 (1974)
27 E. Rabinowitch, Govindjee, *Photosynthesis* (John Wiley & Sons, Inc., New York, 1969)
28 P.F. Moulton, J. Opt. Soc. Am. B **3**, 125 (1986)
29 P.W. Milonni, J.H. Eberly, *Lasers* (John Wiley & Sons, Inc., New York, 1988)